PCCP

ROYAL SOCIETY OF CHEMISTRY

PAPER

View Article Online
View Journal | View Issue

Cite this: *Phys. Chem. Chem. Phys.*, 2020, **22**, 9290

Selective host–guest chemistry, self-assembly and conformational preferences of *m*-xylene macrocycles probed by ion-mobility spectrometry mass spectrometry†

Benjamin A. Link,[a] Ammon J. Sindt,[b] Linda S. Shimizu [b] and Thanh D. Do *[a]

Received 24th December 2019,
Accepted 14th April 2020

DOI: 10.1039/c9cp06938k

rsc.li/pccp

We demonstrated ion-mobility spectrometry mass spectrometry (IMS-MS) as a powerful tool for interrogating and preserving selective chemistry including non-covalent and host–guest complexes of *m*-xylene macrocycles formed in solution. The technique readily revealed the unique favorability of a thiourea-containing macrocycle MXT to Zn^{2+} to form a dimer complex with the cation in an off-axis sandwich structure having the Zn–S bonds in a tetrahedral coordination environment. Replacing thiourea with urea generates MXU which formed high-order oligomerization with weak binding interactions to neutral DMSO guests detected at every oligomer size. The self-assembly pathway observed for this macrocycle is consistent with the crystalline assembly. Further transformation of urea into squaramide produces MXS, a rare receptor for probing sulfate in solution. Tight complexes were observed for both monomeric and dimeric of MXS in which HSO_4^- bound stronger than SO_4^{2-} to the host. The position of HSO_4^- at the binding cavity is a 180° inversion of the reported crystallographic SO_4^{2-}. The MXS dimer formed a prism-like shape with HSO_4^- exhibiting strong contacts with the 8 amine protons of two MXS macrocycles. By eliminating intermolecular interferences, we detected the low energy structures of MXS with collisional cross section (CCS) matching *cis–trans* and *cis–cis* squaramides-amines, both were not observed in crystallization trials. The experiments collectively unravel multiple facets of macrocycle chemistry including conformational flexibility, self-assembly and ligand binding; all in one analysis. Our findings illustrate an inexpensive and widely applicable approach to investigate weak but important interactions that define the shape and binding of macrocycles.

Introduction

Macrocycles possess structural diversity, molecular recognition and complexation properties with emerging applications in material science, chemistry, and drug discovery.[1–7] Characterization of this macrocycle chemistry is rooted in the ability to probe non-covalent coordination and self-assembly of these molecules, both of which pose major challenges for solution-phase analysis. From a practical perspective, macrocycles have varying solubility tolerances and often have their conformational preferences studied through solvent properties and additives.[8,9] However, in many cases, solution-phase techniques such as NMR cannot provide complete structural information due to the rapid exchange among similar conformers yielding unreadable chemical shifts and broad peaks. Another major technique in macrocycle analysis is X-ray crystallography which determines crystal-packing solid-state structures of macrocycles. Crystal structures of ligand-bound macrocycle complexes have revealed both selective and inconspicuous binding of small molecules including neutral solvents, cations and anions.[10,11] These crystalline frameworks serve as templates for designing hierarchical, functional macrocycles.[12–16] Nonetheless, X-ray crystallography samples only a small subset of conformers which can be seen in solution and only represents materials that assemble in crystalline structures.

In an effort to expand the available toolsets for macrocycle analysis, IMS-MS and computational modeling approaches specifically designed for macrocycles have been utilized to investigate conformations and self-assembly.[9,17–19] However, IMS-MS is still very much underexploited in the field of host–guest chemistry. For instance, while IMS-MS has been used to discriminate glucose isomers on the basis of unique chiral noncovalent complexes with amino acids and cations in the

[a] *Department of Chemistry, University of Tennessee, Knoxville, TN 37996, USA. E-mail: tdo5@utk.edu*
[b] *Department of Chemistry and Biochemistry, University of South Carolina, Columbia, SC 29208, USA*

† Electronic supplementary information (ESI) available: Experimental and computational details, additional mass spectral data. See DOI: 10.1039/c9cp06938k

gas-phase,[20,21] such complexes may not exist in solution. Thus, studies of host–guest complexes with macrocycles using IMS-MS have been limited to few macrocycle classes with well-defined topography and chemistry such as cucurbiturils.[22–25] The preservation of non-covalent interactions seen in solution is vital to accurately convey the selective host–guest chemistry of macrocycles. However, the dehydration and charging processes in MS can disrupt weak solution-phase interactions,[26–28] making studies of native host–guest chemistry difficult. Moreover, non-covalent complexes can be formed unselectively as the coulombic and hydrophobic interactions become more accentuated in the gas-phase. Such structures provide little insight into the solution-phase interactions and specificity. For example, sodiated, potassiated, and chlorinated adducts are ubiquitously observed in MS[29] but the binding of these ions to the molecules in solution may be extremely weak or non-existent. This raises an important question. How can we know if the non-covalent complexes captured by MS feature the real solution structures? So far, the pairwise comparisons between theoretical and experimental collisional cross sections (CCSs) have been the main approach to interpret IMS-MS data.[25,30] CCS is the momentum transfer between the analyte ions and the buffer gas molecules (*e.g.*, He or N_2) averaged over all relative thermal energies.[31] Thus, CCS reflects the ion's size, shape and net charge. This quantity is dependent on the nature of the buffer gas and temperature, but independent of instrument types. Experimental CCSs can be compared with theoretical CCSs of model structures from NMR, X-ray crystallography and computational modeling. Because multiple structures can have the same CCS, the ability to obtain meaningful results rely on the sophistication of the modeling approaches.[32] Spectroscopy on mobility-selected[33–35] or mass-selected ions[36] provides invaluable structural information; however, the techniques are still limited to few lab-built instruments. To determine the strengths and weaknesses of IMS-MS in probing non-covalent interactions, well-designed complexes with known interactions should be studied for benchmarks. Thus, macrocycles provide valuable models to serve our purpose as high-quality X-ray crystallographic and NMR data are often available.

In this work, we investigate three structurally similar but chemically distinct *m*-xylene based macrocycles termed MXU, MXT and MXS (see Fig. 1A). These macrocycles have been previously synthesized and characterized by X-ray crystallography and NMR.[11,37,38] The *m*-xylene macrocycles of urea (MXU), thiourea (MXT), and squaramide (MXS) each display various conformers driven by intra- and inter-molecular interactions to afford assemblies of 2D sheets and columnar tubes.[37–39] MXS was previously shown to have high affinity toward SO_4^{2-}.[11] Thus, we revisited the complex to elucidate the driving forces behind the high specificity.[11] With IMS-MS, we are able to probe additional conformers and identify ligand-driven conformational preference that is specific to each macrocycle. Thus, we demonstrate the power and utility of IMS-MS to evaluate macrocycle complexity and selective binding of guest molecules in the gas phase that directly correlates to interactions in solution.

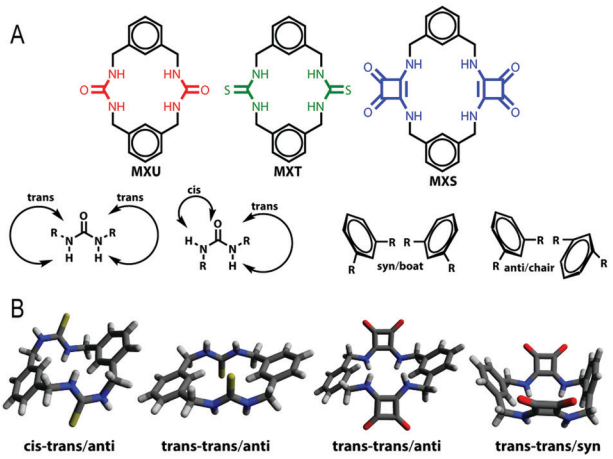

Fig. 1 (A) Chemical structures of MXU (MW = 324 g mol^{-1}), MXT (MW = 356 g mol^{-1}) and MXS (MW = 428 g mol^{-1}). The *cis*/*trans* and *syn*/*anti* configurations of the amines and benzyl groups are shown for MXU. (B) X-ray crystal structures of MXT and MXS showing distinct configurations of amine and benzyl groups.

Materials and methods

Macrocycle synthesis and purification

The MXU, MXT and MXS macrocycles were synthesized according to the previously established procedures.[38] Stock samples were prepared at the concentration of 1 mg/200 μL of DMSO (10 mM). The stock was further diluted 1 : 1000 to the final concentration of 10 μM in either H_2O : ACN (1/1 v/v) or pure H_2O. The choice of solvents has no impact on the CCS measurements, although in a few cases ACN adduction was observed.

IMS-MS. All solvents used in this work were of LC-MS grade. Agilent ESI-L tuning mix ("tune-mix", Agilent, Santa Clara) was purchased and diluted in 95 : 5 v/v ACN : H_2O. Mass spectrometry and multi-field ion-mobility spectrometry experiments were performed using an Agilent 6560 IMS-Q-TOF instrument (Agilent Technologies, Santa Clara, CA). Ions were generated by a dual ESI/Agilent Jet Stream (JS) source and a syringe pump at the rate of 30 μL min^{-1}. Instrument parameters were tuned based on early work by Gabelica and co-workers as previously reported.[9,40,41] The ions were stored in a source funnel and subsequently pulsed into a 78.1 cm drift cell filled with He gas at 3.94 Torr. The ions drift through the cell with velocities proportional to their sizes, shapes and net charges, as the forces created by a weak electrical field on the ions and the drag force due to collisions with buffer gas molecules cancel each other. Drift velocity can be related to the reduced ion mobility K_0, and used to calculate the experimental CCSs σ given in eqn (1)

$$\sigma \approx \frac{(18\pi)^{\frac{1}{2}}}{16}\left[\frac{1}{m}+\frac{1}{m_b}\right]^{\frac{1}{2}}\frac{ze}{(k_B T)^{\frac{1}{2}}}\frac{1}{K_0}\frac{1}{N} \quad (1)$$

where m and m_b are the molecular weights of the ions and buffer gas molecules, respectively, ze is the charge of the ion, N is the buffer gas density. Tune-mix's m/z 922 (CCS_{He} = 175 $Å^2$)[42,43] and m/z 1034 (CCS_{He} = 190 $Å^2$)[42] were used as

reference ions for both mass and CCS accuracy in positive and negative mode, respectively.

Distance geometry modeling and QM optimization. Initial structures of the macrocycles were generated by the Builder/Sketcher module in VIDA v4.4.0.4 starting from a 2D skeletal structure. The macrocycle module in OMEGA v3.0.0.1[44,45] was used to generate ensembles of conformations and clustered based on RMSD. MXT·Zn^{2+} and 2MXT·Zn^{2+}. There are two crystal structures of MXT (see Fig. 1).[38] However, in both cases, the sulfurs are in the *anti*-configuration. We predicted that the sulfurs in the *syn* configuration would maximize the interaction with Zn^{2+}. We used distance geometry (DG) modelling as described before[9] to generate an ensemble of conformations including those with sulfurs in the *syn* position. We then geometrically optimized the complexes of Zn^{2+} and MXT (with sulfurs in both *anti* and *syn* configurations) by density functional theory (DFT) at the B3LYP/def2-svp[46,47] level of theory using Grimme D3 dispersion correction,[48] and the polarizable continuum model (PCM),[49] all available in the Gaussian 09 package.[50] The optimized MXT·Zn^{2+} complex was used to build the initial structure of $[2MXT - H + Zn]^{2+}$. MXS·Cl^- and MXS·NO_3^-. The initial structures were built using the MXS X-ray crystal structure (*trans–trans*/*anti*; ''chair'' see Fig. 1 in the main text) from the Shimizu group.[38] This is the X-ray structure without any ligand. We didn't start with the MXS·SO_4^{2-} crystal structure from the Jolliffe group[11] as we did not want to bias the conformation toward the *trans–trans*/*syn* (''boat'', Fig. 1) conformation. The structures were optimized using the same DFT method described above. DG modelling was also performed to generate an ensemble of neutral MXS. As described in the following section, a small number of conformations were selected for further geometry optimization with DFT and generate the deprotonated species. Because the $[M - H]^-$ species were formed in the gas phase, QM calculations were performed without any solvation model.

Theoretical CCS calculations. Theoretical CCSs were obtained using the trajectory method (TJ) available in the Mobcal package.[51,52]

Results and discussion

To analyze the adoption of different possible conformations for the *m*-xylene macrocycles, we note the possible arrangement of amine groups and benzyl rings as these specific arrangements could provide stability to the structures. In Fig. 1A, the 2D skeletal structures of MXU, MXT, and MXS are all presented. Directly below, the steric classifications of structure about the nitrogen are represented using MXU as an example. In each case, the R-group represents the attached *m*-xylene group, and *cis*/*trans* are defined strictly by the orientation of the constituent in reference to the associated *m*-xylene. Ultimately, each structure carries specific reference to the *cis*/*trans* nature of the amine groups.

Following the classification of the sterics surrounding the amine-nitrogen, there needs to be definition surrounding the orientation of the *m*-xylene itself. The orientation of the *m*-xylene groups give rise to the classification of structures as chair *versus* boat conformations. Therefore, for each macrocycle, there are multiple structural isomers, of which *cis–trans*/*anti*, *cis–trans*/*syn*, *trans–trans*/*anti* and *trans–trans*/*syn* have been experimentally observed.[11,37,38] The *anti*-configuration favors intermolecular interactions whereas the *syn*-configuration maximizes intramolecular forces. If the orientations of the urea/thiourea/squaramide groups are also considered, then there would be a total 12 possible isomers (not counting structures with amines in mixed configurations). Ring strain may render some of these conformations energetically unfavorable. Of note, only two isomers of the *m*-xylene macrocycles were reported in previous studies (*e.g.* MXT,[38] MXS[11]). According to the X-ray data, the *trans–trans* conformations were dominant.

MXT shows high affinity toward nitrate (NO_3^-) and zinc (Zn^{2+}) complexation

Utilizing IMS-MS, the analysis of MXT was conducted in positive and negative electrospray ionization (ESI) polarity to produce the mass spectral data shown in Fig. 2. Fig. 2A shows the mass spectral data of MXT in negative mode, which contains peaks associated with molecules resulting from the loss of a hydrogen ($[MXT - H]^-$; *m*/*z* 355) or an addition of a chloride to a neutral MXT ($[MXT + Cl]^-$; *m*/*z* 391). But neither of them is the most intense mass spectral peak which is at *m*/*z* 418. The mass difference between this *m*/*z* 418 species and the neutral MXT (MW = 356) is 62. The only molecule (anion) with the MW of 62 is nitrate (NO_3^-). The monoisotopic mass of $[MXT + NO_3]^-$ is 418.1008 and the observed mass is 418.0996 (−2.8 ppm difference; running a mass calibration before data acquisition can reduce the mass accuracy to 0.7 ppm). The source of nitrate could be from the LC-MS water or a slow conversion of ammonium into nitrate occurring inside that nebulizer that we could not completely remove. Another possible mechanism for NO_3^- formation in the source is by the corona discharge *via* the reactions between N_2 and O_2 from the sheath gas.[53] As shown below, MXT is the only macrocycle of the three that shows a strong binding to nitrate. We note that since chloride and nitrate have low hydration energies ($\Delta G = -347$ kJ mol^{-1} and -306 kJ mol^{-1}, respectively), they could bind unselectively to many macrocyclic hosts. However, the intensity of the *m*/*z* 418 peak suggests a strong interaction between MXT and NO_3^-.

The discovery of selective Zn^{2+} binding to MXT is serendipitous. As shown in Fig. 2B (a mass spectrum of MXT in positive mode), there are two small peaks at *m*/*z* 419 and 775. We note that from the monoisotopic masses, these peaks cannot be $[MXT + ACN + Na]^+$ (*m*/*z* 420) and $[2MXT + ACN + Na]^+$ (*m*/*z* 776). At first glance, the acetonitrile–sodium complexes are highly probable because we used a small amount of ACN to assist the dissolution of MXT, and Na^+ is ubiquitous in MS. However, the mass difference (1 amu; we ran the sample with a tune-mix ion with known exact mass to ensure no mass shift) and the isotope patterns both suggest that the peaks at *m*/*z* 419 and 775 are not acetonitrile adducts, but are instead due to MXT complexing with Zn^{2+} ($[MXT - H + Zn]^+$ at *m*/*z* 419 and $[2MXT - H + Zn]^+$ at *m*/*z* 775). In these

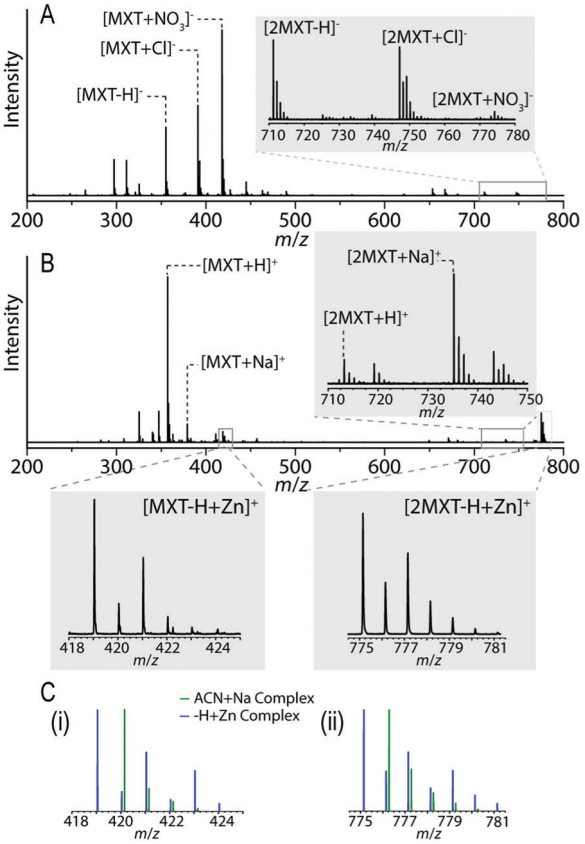

Fig. 2 (A and B) Negative and positive ESI-mass spectra of MXT in H_2O. (C) Theoretical isotope patterns of MXT in complexed with ACN and Na^+ (green) and with Zn^{2+} (blue).

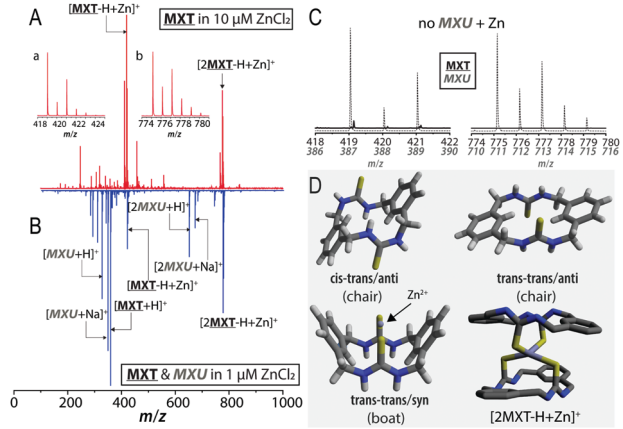

Fig. 3 (A and B) Representative mass spectra of MXT in 10 μM $ZnCl_2$ (red), and of equal molar MXT and MXU in 1 μM $ZnCl_2$ (blue). (C) Partial mass spectral regions showing no MXU (solid) and Zn (dotted line) complexation. (D) The X-ray crystal structures of MXT (top; taken from Sindt *et al.* (2018)) and the QM structure of MXT + Zn obtained using distance geometry and B3LYP calculation. The MXT + Zn structure was used to build and further optimize 2MXT + Zn. In the last structure, the hydrogens are omitted and Zn–S bonds are shown to illustrate the tetrahedral coordination.

complexes, the MXT elects to remove a proton and houses the zinc as its guest. We ran several samples with Zn^{2+} during the period when the data were collected, so there could have been residual Zn^{2+} in the nebulizer, and thoroughly cleaning the nebulizer did remove the peaks. To better exemplify zinc cation interaction, direct introduction of more zinc ions ($ZnCl_2$) into the samples was performed and reported in Fig. 3A. The sample containing 10 μM $ZnCl_2$ and 10 μM MXT shows a drastic increase in the intensity of the same the monomeric and dimeric MXT–zinc peaks (*m*/*z* 419 and 775). Both intense mass spectral peaks exhibit the same isotope patterns (panels a and b) in agreement with the data in Fig. 2B and C.

The "deprotonation" of MXT in positive ESI mode is intriguing. While it is common to observe multimers of biomolecules at lower charge states than the expected charges calculated based on the native charge state of the monomer,[54,55] such deprotonation is unlikely caused by ESI. As pK_a of charged amino acids are often affected by the local environment, the low charge-state multimers are formed in solution to avoid charge repulsion. On the other hand, the deprotonation of MXT cannot occur in solution. In other words, the complexes existed as doubly charged species in solution, which were later deprotonated to singly charged in positive ESI. Presumably, the deprotonation is necessary to preserve these complexes in the gas-phase as we didn't observe the z = +2 species. We speculate that there are intermediates that contain Cl^-, and when the Cl^- is dissociated from the complex, it takes a proton from MXT. We are currently investigating this hypothesis by studying *m*-xylene macrocycles with mixed urea and thiourea substituents.

Finally, to illustrate the uniqueness of the MXT–zinc interaction, MXT and MXU were introduced simultaneously in a solution of 1 μM $ZnCl_2$ (Fig. 3B). The same mass spectral peaks corresponding to MXT and Zn complexes are clearly observed. However, MXU, which is chemically identical to MXT except the sulfurs were replaced by oxygens, does not show any affinity to Zn^{2+}. In fact, MXU prefers to form complexes with Na^+, a gas-phase mediated process. In Fig. 3C, we show the *m*/*z* regions where $[MXU - H + Zn]^+$ and $[2MXU - H + Zn]^{2+}$ should be found. The signals are below the noise level, indicating that MXU does not take Zn^{2+} as its ligand. Thus, the selective interaction of MXT and Zn is solely due to soft–soft Zn–S interactions. QM modeling of MXT·Zn^{2+} at the 1 : 1 ratio shows that the binding induces the MXT macrocycle to adopt the boat conformation (see Fig. S1, ESI†). At the 2 : 1 ratio, the two "boat" MXT molecules become "unfolded" and further stabilize the Zn cations to form 2MXT·Zn^{2+} as shown in Fig. 3D. Note that starting from the same initial structures, QM optimization of both $[2MXT + Zn]^{2+}$ and $[2MXT - H + Zn]^+$ successfully completed producing structures with the same backbone (see the PDB files in the ESI†). We note that in the same experiment, we observed $[3MXT + H]^+$ at *m*/*z* 1069 but not any Zn bound to MXT trimer, indicating that Zn coordination is specific to MXT monomer and dimer. The dimeric $[2MXT - H + Zn]^+$ complex consists of two off-axis "flat" MXT molecules with four sulfurs equally "bonded" to the Zn. Such offset is crucial for the sulfur coordination around the Zn cation to be in a distorted tetrahedral geometry,[56] with an average Zn–S distance of 2.5 Å. The tetrahedral geometry is found in sphalerite ZnS or Zn^{2+} ligands

within proteins.[57] The typical tetrahedral Zn–S bond distance in proteins lies between 2.2 and 2.4 Å.[57,58] The theoretical CCS of the structure is 177 Å^2, is in a good agreement with the experimental CCS; 175 Å^2. This finding is particularly exciting because it demonstrates that MXT promotes unique supramolecular chemistry that mimics Zn coordination in crystal lattice and biological systems and can be used to distinguish Zn^{2+} from other divalent metals.

MXU shows high-order oligomerization following columnar assembly, along with DMSO complexation

Following the previous order of analysis, negative and positive mass spectra of MXU in water are reported in Fig. 4A and B, respectively. Similar to MXT, MXU also shows negatively charged adducts with chloride (*e.g.*, $[MXU + Cl]^-$; *m*/*z* 359), as well as negatively charged species corresponding to deprotonation ($[MXU - H]^-$; *m*/*z* 323).

However, the unique property of MXU is found in its ability to coordinate its assembly with DMSO. DMSO was present in all of our samples because we used this solvent to prepare the stock samples. In Fig. 4A and B, DMSO is shown to be present in MXU structures from monomer up to the trimer state in negative mode. Meanwhile, since DMSO is a neutral molecule, the detection of MXU in complex with DMSO should not be limited to negative ESI polarity only. In other words, we should be able to capture the same complexes in positive mode.

Fig. 4B, representing the positive mode MS data of MXU, shows a vast array of distinguishable oligomers. Aged solutions of MXU forms oligomeric structures up to the hexamers. In order to differentiate and identify mass spectral peaks, it is important to realize the importance of isotope spacing as an indicator of charge state (*i.e.*, the isotope spacing of 0.5 *m*/*z* indicates the charge state of +2 while the spacing of 1.0 *m*/*z* indicates *z* = +1). An example of isotopic spacing determining the assignments of MXU clusters is shown in Fig. S2 (ESI†). Along with the negative mode, MXU is shown again to form complexes with DMSO solvent, which is seen in every degree of oligomerization shown. Thus, DMSO is an example of guest molecule that binds tangentially to MXU and does not affect the self-assembly of the macrocycle. Because there is no X-ray crystal structure of MXU with DMSO, we performed QM calculation of 2MXU·DMSO. In the initial structure, DMSO was loosely placed on the top of the crystallographic MXU dimer. The optimized structure showed that DMSO was bound to MXU *via* a weak electrostatic interaction between nucleophilic DMSO's oxygen and one set of *trans–trans* amines of MXU (see Fig. S3, ESI†). The motif is similar to the crystal structure of MXS·DMSO by Jolliffe[11] and is discussed in the next section.

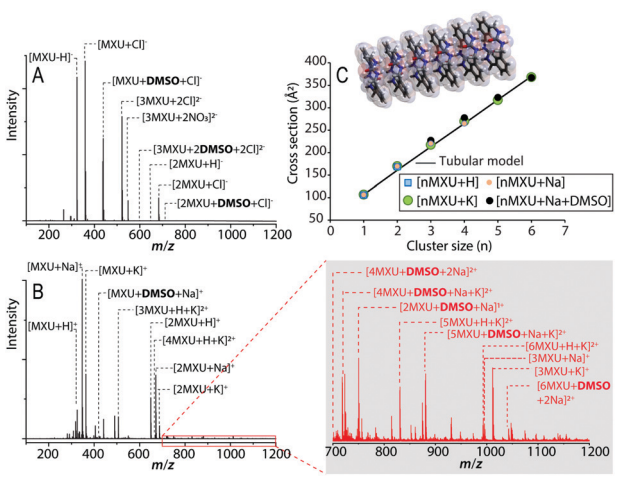

Fig. 4 (A and B) Representative mass spectra of MXU in positive and negative mode, respectively. A zoom-in partial mass spectrum showing MXU clusters is shown with major peaks labelled. (C) A plot of cluster size (*n*) *vs.* experimental CCSs. The tubular model was built based on the X-ray crystal structures.

To further verify the formation of high-order oligomers, IMS-MS data were compared to X-ray crystallography data.[37] As shown in Fig. 4C, the columnar model of MXU self-assembly, taken from previously reported X-ray data, is compared to the experimental CCSs. Previous studies on self-assemblies of biomolecules such as amyloid proteins indicated that the experimental CCSs correlated well with the X-ray structures.[59]

Here, the experimental CCSs include those of bare ions, sodiated and potassiated adducts, as well as their complexes with DMSO. Not only is the formation of these higher-order oligomers validated from the monomer to the hexamer, but it also confirms that they followed this specific self-assembly model. We note that the oligomer formation was only observed in weeks-old samples incubated at room temperature. Fresh samples did not show oligomers larger than dimer, suggesting that the oligomer formation is time-dependent and not driven by the ESI process. Because our MS samples had a much lower concentration (~μM) than required for NMR studies (mM), partially due to the poor solubility of MXU in water, traditional experiments such as DOSY NMR could not be performed. At the same time, it is well-established by X-ray crystallography that this macrocycle forms nanotubes.[37] In the previous study, the MXU crystals were grown in a sealed pressure tube using superheated glacial acetic acid. The crystals formed as the system was slowly cooled from 135 °C to 25 °C with the key window of formation from 135 to 100 °C.[37] Thus, while the high temperature in the ESI source can change the distributions in solution at room temperature, the X-ray conditions suggest that (a few seconds of) sample heating in ESI should not affect the oligomerization leading to nanotube formation.

The columnar model allows for parallel displaced π-stacking of *m*-xylene rings and head-to-tail arrays based on 3-centered urea hydrogen bonds. The latter arises from the interaction of the NH's of one urea to the carbonyl of another urea on an adjacent molecule. Both the π-stacking and urea hydrogen bonds contribute to the stability of high-order oligomers.[37] Furthermore, based on the experimental CCSs, the difference between potassiated and sodiated adducts and the bare ions (see Fig. 4C and Table S2, ESI†) is negligible, indicating there is no conformational transition, consistent with the fact that the binding is unselective.

In the case that the high-order oligomers are formed, it is important to address how the arrival time distributions (ATDs)

of oligomers can show evidence for high-order oligomers in a nontraditional way. In particular, post IM dissociation events in the absence of collision induced dissociation (CID) show the presence a feature with much longer arrival time than expected. For example, when a singly charged dimer of MXU passes through the drift tube, there is the possibility of a neutral MXU loss yielding a singly charged monomer that has the mobility of a dimer. When this happens, the ATD of the smaller fragment will show an additional feature at a much longer arrival time. That arrival time is slightly shorter (~0.1 ms) than the arrival time of the precursor species. Fig. 5 shows an example of MXU, and the same phenomenon occurred for all three macrocycles. In Fig. 5, the $[MXU + H]^+$ feature at 16.54 ms (panel a) has a similar arrival time to that of $[2MXU + H]^+$ at 16.71 ms (panel d).

Binding of sulfate HSO_4^- to MXS probed by IMS-MS

MXS was originally designed by the Jolliffe group to be a sulfate receptor.[11] Their study, which employed NMR and X-ray crystallography, showed that SO_4^{2-} binds to MXS in a 1:1 fashion.[11] The Shimizu group revisited MXS and solved a crystal structure of pure MXS without SO_4^{2-}.[38] The data suggested that MXS alone preferred *trans–trans/anti* whereas its complex with sulfate promoted *trans–trans/syn* (see Fig. 1B). This chair to boat transition indicates that the anion preferentially maximizes their interactions with amine NH protons.

In our IMS-MS experiment (Fig. 6), we evaluate the formation of $MXS{\cdot}SO_4^{2-}$ complexes and the competition between SO_4^{2-} and other ubiquitous anions such as Cl^- and NO_3^- or neutral solvent such as DMSO. Fig. 6A and B shows the ESI mass spectra with and without SO_4^{2-} in negative polarity. In the absence of sulfate, we observe mass spectral peaks corresponding to the complexes of MXS with Cl^- (*m*/*z* 463), with NO_3^- (*m*/*z* 490), and with DMSO (*m*/*z* 541). The $MXS{\cdot}SO_4^{2-}$ complex at *m*/*z* 525 ($[MXS + H + SO_4]^-$) is observed at 0.1 μM of SO_4^{2-}, which is equivalent to the ratio of MXS to SO_4^{2-} of 100:1. This mass spectral peak grows drastically as the concentration of SO_4^{2-} is increased. Starting at 10 μM of SO_4^{2-}, we also observe the complex of dimeric MXS with a single SO_4^{2-} (*m*/*z* 953; $[2MXS + H + SO_4]^-$). Fig. 6C summarizes the relative intensities of the bare MXS monomer, MXS dimer and their corresponding SO_4^{2-} complexes. At 10 μM of SO_4^{2-}, the sulfate complexes are prevalent; there is no sign of chlorinated and nitrated species. Fig. 6C shows the relative MS intensities of four major species: $[MXS - H]^-$ at *m*/*z* 427, $[2MXS - H]^-$ at *m*/*z* 855, $[MXS + H + SO_4]^-$ at *m*/*z* 525, and $[2MXS + H + SO_4]^-$ at *m*/*z* 953. The intensity of the monomer complex increases as SO_4^{2-} concentration is increased from 0.1 to 10 μM. After that,

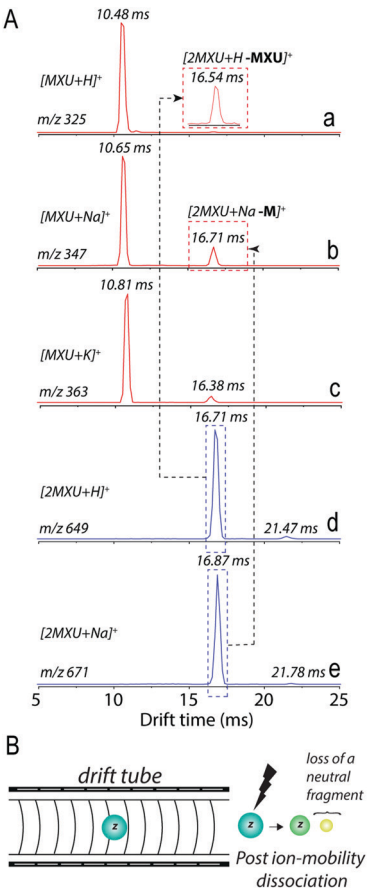

Fig. 5 (A) Post-IM dissociations observed in the ATDs of MXU monomers and dimers. (B) A schematic illustration of the process. The dissociation occurred without CID.

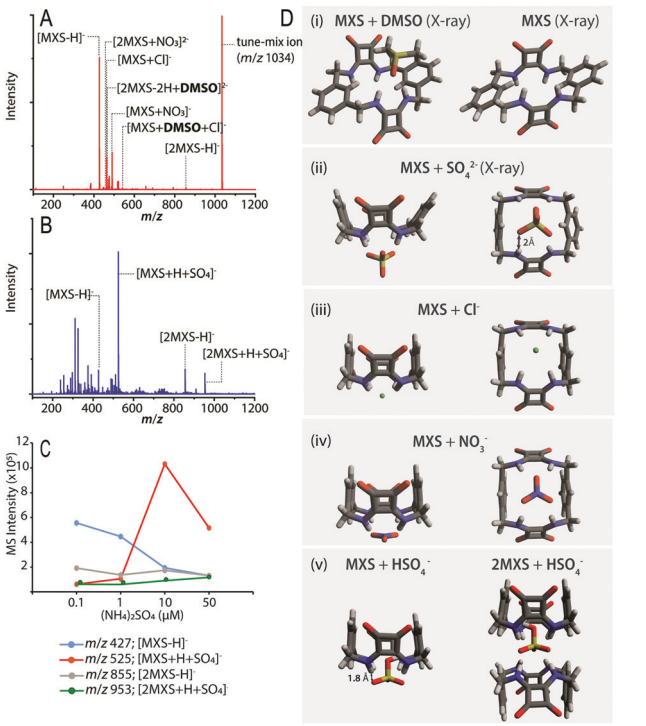

Fig. 6 (A and B) Representative mass spectra of MXS with and without SO_4^{2-} (50 μM). (C) A plot of relative MS intensities of four major species: bare MXS monomer, bare MXS dimer, sulfate bound monomer and sulfate bound dimer. (D) (i and ii) X-ray crystal structures of MXS in complex with DMSO and SO_4^{2-} taken from Qin *et al.* (2016). (iii and iv) QM structures of MXS in complex with Cl^- and NO_3^-. (v) QM structures of MXS monomer and dimer in complex with HSO_4^-.

the intensity of the peak decreases to give way for more of the dimeric complex.

In Fig. 6D(i and ii), the X-ray crystal structures of MXS with and without DMSO or SO_4^{2-} obtained by the Jolliffe and Shimizu groups are shown. DMSO is loosely bound to the macrocycles (MXU and MXS) and does not affect the host conformation. On the other hand, sulfate SO_4^{2-} induces the macrocycle to adopt the *trans–trans/syn* (boat) conformation.

In our experiments, we observed $[MXS + H + SO_4]^-$ and $[2MXS + H + SO_4]^-$ but not $[MXS + SO_4]^{2-}$ or $[2MXS + SO_4]^{2-}$. As in the case of MXT and Zn^{2+}, it is possible that protonation can occur in negative ESI mode. That is, the species existed in solution have $z = -2$ charge state. However, this leads us to an important question. How is the binding of SO_4^{2-} to MXS different from NO_3^- and Cl^-? We performed QM modeling of MXS·Cl^- and MXS·NO_3^- (Fig. 6D(iii and iv)) starting from the X-ray crystal structure (*trans–trans/anti*; chair) to avoid conformational bias to the boat conformation. The optimized geometry of both complexes is *trans–trans/syn* (boat), suggesting that anions share the common interaction with MXS (*via* coulombic interactions between the anion and amine protons).

Given the structures shown in Fig. 4D and E, it is unclear how SO_4^{2-} could have a much higher affinity to MXS than NO_3^-.[11] Both anions interact with the host *via* three negatively charged oxygens. The average distance between MXS's amine proton and the anion's oxygen is 2 Å. As mentioned above, there are two possibilities: (a) the MXS complex was protonated (in the gas phase), or (b) the sulfate in binding mode exists as HSO_4^-. To evaluate both possibilities, we performed QM calculations on $[MXS^{1+} + SO_4^{2-}]$ and $[MXS^0 + HSO_4^-]$. Interestingly, both calculations yielded the final structure of $[MXS + HSO_4^-]$ in which the OH of HSO_4^- inserted into the cavity of MXS. Of note, hydrogen atoms only scatter X-ray radiation weakly and hence it is difficult to locate them accurately in X-ray crystal structures.[60] In the original study by the Jolliffe group, the K_a (apparent stability constant) for MXS·HSO_4^- was not given because the data could not be fitted to a binding model.[11] Furthermore, in the X-ray structure, the anionic complex is "nestled" between the pendant residues of a pair of tetrabutylammonium cations,[11] but those additives are not part of the system studied by IMS-MS here (we used ammonium sulfate). In our proposed orientation (Fig. 6D(v)), all four oxygens of HSO_4^- were making contact with the MXS host, and notably the (sulfate)O–(squaramide)N distance is reduced to 1.8 Å. Therefore, the preferred ligand of MXS is likely HSO_4^-, and not SO_4^{2-}. Moreover, this binding motif is not favorable without the sulfate OH. At the dimer stage, our QM calculations show that $[(2MXS + H) + SO_4]^-$ is about 5 kcal mol^{-1} higher in energy than $[2MXS + HSO_4]^-$. The experimental CCSs of $[MXS + HSO_4]^-$ and $[2MXS + HSO_4]^-$ are 136 $Å^2$ and 206 $Å^2$, respectively, which are in agreement with the theoretical CCSs of 133 $Å^2$ and 216 $Å^2$. Therefore, IMS-MS provides an important characterization of the protonation state and interaction motif of the sulfate guest which could have been difficult to capture by traditional solution-phase technique.

However, we cannot exclude the possibility that the protonation occurred in positive ESI mode leading to our observation of MXT:HSO_4^- complexes instead of MXS:SO_4^{2-} as previously reported. The protonation step is a subject of future investigation, but it shows that our knowledge of the ESI process is incomplete. Nonetheless, our IMS-MS data and previous NMR/X-ray data[11] both indicate that sulfate has a higher affinity to MXS than other ubiquitous anions such as chloride and nitrate.

The conformational preference of MXS probed by IMS-MS

As discussed above, the conformations of macrocycles could be altered by the guest molecules in addition to competition between intra- and inter-molecular interactions induced by the local environment. Our modeling data and previous X-ray data[11,37,38] collectively suggest that anion guests (Cl^-, NO_3^-, SO_4^{2-}) preferentially drive the macrocycles to adopt the *trans–trans/syn* (boat) conformation and bind to the amine protons. X-ray data also showed that neutral guests such as DMSO do not affect the conformations of the macrocycles as much. It is worthy to mention that although MXT, MXU and MXS are able to form complexes with nitrate, the ratios of $[MXT + Cl^-]$/$[MXT + NO_3^-]$ suggest that MXT has the strongest interaction. For the same motif of interactions, QM calculations reveal that the amine protons in MXT have slightly more positive partial charges than both MXS and MXU. Thus, the *m*-xylene substituents can indirectly affect the binding of anions by controlling the partial charges on these protons.

One may question the effect of protonation or deprotonation on the conformations of the macrocycles. Previous high-level QM calculations showed that the positively charged protons should reside on the urea oxygens or thiourea sulfurs.[61] In addition, there is no significant difference (2–3%) between the experimental CCSs of $[M - H]^-$, $[M + H]^+$, $[M + Cl]^-$ and $[M + Na]^+$ (M = MXT or MXU). Protonation or deprotonation, in the case of MXU and MXT, tend to compact the molecules yielding smaller CCSs than the neutral species. This contraction is expected and often small ($< 5\%$) (see Fig. S4, ESI† for the CCSs of neutral, protonated and deprotonated MXT conformations as an example).

However, MXS behaves rather differently from the other two macrocycles. Since MXS ionizes much better in negative than in positive mode, we limit our discussion here to negative mode, and the positive mode data can be found in the ESI.† The theoretical CCSs of MXS crystal structures (Fig. 6D with the ligands removed) are 140 $Å^2$ (chair) and 135 $Å^2$ (boat conformation). Given that it is possible for the trajectory method to overestimate the CCSs, our experimental CCSs of $[MXS + Cl]^-$ (130 $Å^2$) does not seem to set out any contradiction, and based on CCS alone, the species we probed in the gas-phase is likely the boat conformer. However, the deprotonated MXS ($[MXS - H]^-$) has an experimental CCS significantly smaller (σ_{exp} = 119 $Å^2$ *vs.* 130 $Å^2$ of chlorinated MXS; 8% smaller). To put it in perspective, MXS is significantly larger than MXU (two squaramides *vs.* two oxygens), but the experimental CCS of MXU is already 114 $Å^2$. In addition, the drift time at *m*/*z* 427 corresponding to $[M - H]^-$ resolves at least three features: two monomers and one dimer based on isotope spacings (Fig. 7). The less dominant monomer has a similar CCS (134 $Å^2$) to the

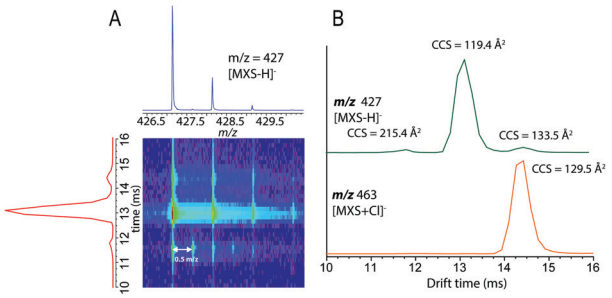

Fig. 7 (A) 2D plot of *m/z* vs. drift time (ms) for $[MXS - H]^-$ showing three features corresponding to one dimer and two monomers. (B) Representative ATDs of $[MXS - H]^-$ and $[MXS + Cl]^-$.

chlorinated MXS (130 Å^2), and to the boat X-ray conformation (135 Å^2). The observation of the three features is independent from the buffer gases (helium or nitrogen). The difference between the two monomeric features is too small for one of them to be a post-IM dissociated product (see the discussion on this issue above). At first glance, the two conformers could be the charge isomers (protomers) for which a few examples have been reported in the literatures (*e.g.*, the N- and O-protonated isomers of benzocaine).[62] However, QM calculations could not reveal the two protomers of MXS. The negative charge is divided among the amine nitrogens and the squaramide oxygens. Furthermore, the difference in experimental CCSs of benzocaine isomers is 20 Å^2 ($\sim$14%)[62] whereas our case of MXS, the difference is only 8%.

In order to determine whether the 8% difference in CCS is due to conformations, we need to thoroughly sample possible conformations of MXS. DG provides an inexpensive and robust method to complete this task.[9,63] We generated 200 distinct conformations of MXS, and grouped them into 40 clusters. The clusters span a wide range of possible conformations. The theoretical CCSs of these clusters are shown in Fig. 8. There are some interesting conformations. The first one (termed **C1** here) is another boat conformation with the two squaramides

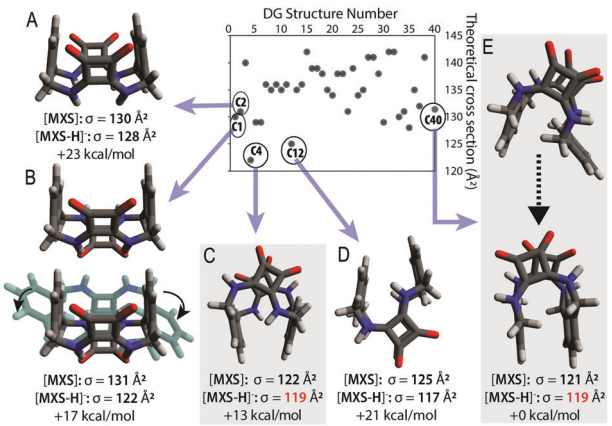

Fig. 8 Results from DG modelling of MXT. (A–E) Clusters **C1**, **C2**, **C4**, **C12**, and **C40**; the B3LYP optimized **C40** structure has the lowest energy in the gas-phase while **C4** has the lowest energy in solution. The relative energy in vacuum is shown.

anti to each other. This conformation is structurally similar to and lower energy than the *trans–trans/anti* conformation **C2** (Fig. 8A) obtained from the X-ray crystal structure of MXS with sulfate.[11] As the two benzyl groups of *m*-xylene of **C1** rotate to maximize the intermolecular packing, the solid-state conformation of bare MXS by Shimizu and co-workers[38] could be obtained (Fig. 8B). In addition, there are 3–4 clusters with CCSs smaller than 130 Å^2 as they might be the conformation(s) probed in the experiment. Notably, clusters **C4** and **C12** (Fig. 8C and D) have theoretical CCSs of 122 and 125 Å^2, respectively, much closer to the experimental CCS of the dominant MXS monomer (σ_{exp} = 119 Å^2). Interestingly, both of these clusters have the amines in *cis–trans* positions. The *cis–trans* amines may be structurally less favorable than *trans–trans*[38] or *cis–cis*[64] in forming inter-molecular interactions such as hydrogen bonding or π-stacking, but can promote intra-molecular interactions. We also searched for MXS structures in which both squaramides-amines are *cis/cis*, and there was only one structure (**C40**). QM optimization of **C40** yielded a U-shaped, low-energy structure with the theoretical CCS in a close agreement with the experimental data. The optimized **C40** (Fig. 8E) has the lowest energy in the gas-phase while **C4** has the lowest energy in solution. The *cis–trans* and *cis–cis* configurations allow for maximum intra-molecular interactions including the stackings of the pair squaramides and of the two benzyl rings.

We further optimized the deprotonated form of the five structures, and recomputed the theoretical CCSs. Similar to MXT and MXU, deprotonation compacts but does not change the conformation (see Fig. S5, ESI†). The structures **C4** and **C40** in the $[M - H]^-$ form have the same CCS of 119 Å^2, which is identical to the experimental CCS of the dominant feature. The fact that IMS-MS is able to sample low energy conformations that were not reported by NMR or X-ray crystallography indicates that IMS-MS is a valuable and complementary technique in macrocycle structural characterization. Nonetheless, this is expected because as the molecules are brought into the gas phase, external interferences by crystal packing or ensemble average can be eliminated.

Summary and conclusions

Advances in synthetic methodology along with the emergent need for confining diverse functional groups in a small molecular structures have driven the exploration of new macrocyclic molecules. These molecules occupy unique chemical spaces and form functional and complex host–guest chemistry. To be able to investigate the complexes by native IM-MS, a prerequisite is to be able to ionize the complex without destroying it, and if the goal is to study the solution structure, without perturbing it. Random associations, driven by strong coulombic and hydrophobic interactions in vacuum, can lead to detection of non-covalent complexes that do not represent solution-phase structures. To address this issue, the first step is to examine the possibility that selective complexes of non-covalent host–guest

chemistry could be detected. This work investigates three major aspects of macrocycle chemistry: ligand binding, self-assembly and conformational analysis. Using three *m*-xylene macrocycles that were previously characterized by NMR and X-ray crystallography,[11,37,38] we demonstrated that IMS-MS, assisted by DG and QM calculations, can sample both unspecific and specific host–guest complexes of these macrocycles with anions and cations. A clear example is the dimer complex of MXT with Zn^{2+}, which resembles Zn–S interactions in tetrahedral ZnS. Another example is the complex of MXS and sulfate. Sulfate was able to outcompete ubiquitous ions in solution such as Cl^- to form complex with MXS host, and our data suggest that sulfate binds tighter to MXS in the form of HSO_4^-. Overall, our data provide compelling evidence that native IMS-MS can probe selective host–guest chemistry in macrocycles and reveal new, exciting chemistry.

All three macrocycles studied in this work have poor water solubility. Previous structural characterizations in solution were limited to a small number of solvents (*e.g.*, acetic acid, DMSO). The macrocycle conformations are determined by solvent properties, additives (or guest molecules) and remote substituents. Sophisticated X-ray crystallography and NMR analysis of *m*-xylene macrocycles suggested the structural complexity of these systems. However, IMS-MS methods were remarkably informative and revealed additional low-energy conformations, placing all of these discrete structures onto a complete conformational landscape.

Computational modeling of macrocycles is not yet a mature technique. Major developments in this technique rely on X-ray crystal structures,[65–67] even though crystallography and modeling often do not aim to sample the same structures. Many of X-ray crystal structures are high-energy conformations in a low-energy solid-state packing. In the case of MXS, we reveal that the low(er) energy (than X-ray structure) conformation could be captured by IMS-MS. Although it is not always necessary to obtain the lowest energy conformations in all cases,[68] our findings offer an alternative, inexpensive, and complementary approach to macrocycle conformational sampling. We expect novel chemistry to be unraveled and fundamentally contribute to our understanding of this unique class of emerging molecules.

Lastly, by investigating a set of *m*-xylene macrocycles with high-quality NMR and X-ray crystallography data, we demonstrated that when the preferred guest molecules are present, they are able to outcompete the ubiquitous ions such as Cl^-, Na^+, and K^+ to form stable complexes with the macrocycles. Our data suggest that IMS-MS, together with computational modeling, provides a robust platform to screen and examine host–guest chemistry of macrocycles. Finally, our work showed that deprotonation could occur in the positive mode ESI, and protonation may also occur in the negative mode, implying that our knowledge of the ESI process is incomplete.

Conflicts of interest

There are no conflicts to declare.

Acknowledgements

We gratefully acknowledge the laboratory start-up research support from the University of Tennessee and Department of Chemistry, the Global Academic Support Program from Agilent, and an academic license for molecular modeling toolkits from OpenEye Scientific, Inc. This work was supported in part by National Science Foundation CHE-1904386 (L. S. S.). We thank Dr. Paul Hawkins at OpenEye, Prof. Roy Sharani at UT, and Prof. Christian Bleiholder at Florida State University for useful discussion.

Notes and references

1 E. Marsault and M. L. Peterson, *J. Med. Chem.*, 2011, **54**, 1961–2004.
2 S. D. Appavoo, S. Huh, D. B. Diaz and A. K. Yudin, *Chem. Rev.*, 2019, **119**, 9724–9752.
3 E. M. Driggers, S. P. Hale, J. Lee and N. K. Terrett, *Nat. Rev. Drug Discovery*, 2008, **7**, 608–624.
4 J. Mallinson and I. Collins, *Future Med. Chem.*, 2012, **4**, 1409–1438.
5 Z. Liu, S. K. M. Nalluri and J. F. Stoddart, *Chem. Soc. Rev.*, 2017, **46**, 2459–2478.
6 D. L. Selwood, *Chem. Biol. Drug Des.*, 2017, **89**, 164–168.
7 A. K. Yudin, *Chem. Sci.*, 2015, **6**, 30–49.
8 S. Hoger, D. L. Morrison and V. Enkelmann, *J. Am. Chem. Soc.*, 2002, **124**, 6734–6736.
9 I. W. Haynes, G. C. Wu, M. A. Hague, H. Li and T. D. Do, *Anal. Chem.*, 2019, **91**, 13439–13447.
10 S. Sasaki, M. Mizuno, K. Naemura and Y. Tobe, *J. Org. Chem.*, 2000, **65**, 275–283.
11 L. Qin, A. Hartley, P. Turner, R. B. P. Elmes and K. A. Jolliffe, *Chem. Sci.*, 2016, **7**, 4563–4572.
12 B. A. DeHaven, D. W. Goodlett, A. J. Sindt, N. Noll, M. De Vetta, M. D. Smith, C. R. Martin, L. Gonzalez and L. S. Shimizu, *J. Am. Chem. Soc.*, 2018, **140**, 13064–13070.
13 A. J. Sindt, M. D. Smith, S. Berens, S. Vasenkov, C. R. Bowers and L. S. Shimizu, *Chem. Commun.*, 2019, **55**, 5619–5622.
14 S. I. Stupp and L. C. Palmer, *Chem. Mater.*, 2014, **26**, 507–518.
15 J. M. Lehn, *Proc. Natl. Acad. Sci. U. S. A.*, 2002, **99**, 4763–4768.
16 L. S. Shimizu, S. R. Salpage and A. A. Korous, *Acc. Chem. Res.*, 2014, **47**, 2116–2127.
17 W. Zhang, A. Abdulkarim, F. E. Golling, H. J. Räder and K. Müllen, *Angew. Chem., Int. Ed.*, 2017, **56**, 2645–2648.
18 Y. T. Chan, X. Li, M. Soler, J. L. Wang, C. Wesdemiotis and G. R. Newkome, *J. Am. Chem. Soc.*, 2009, **131**, 16395–16397.
19 W. Zhang, M. Quernheim, H. J. Rader and K. Mullen, *Anal. Chem.*, 2016, **88**, 952–959.
20 G. Nagy and N. L. B. Pohl, *J. Am. Soc. Mass Spectrom*, 2015, **26**, 677–685.
21 M. M. Gaye, G. Nagy, D. E. Clemmer and N. L. Pohl, *Anal. Chem.*, 2016, **88**, 2335–2344.
22 P. Montes-Navajas, A. Corma and H. Garcia, *ChemPhysChem*, 2008, **9**, 713–720.

23 N. E. de Almeida, T. D. Do, M. Tro, N. E. LaPointe, S. C. Feinstein, J. E. Shea and M. T. Bowers, *ACS Chem. Neurosci.*, 2016, **7**, 218–226.
24 M. Oeren, E. Shmatova, T. Tamm and R. Aav, *Phys. Chem. Chem. Phys.*, 2014, **16**, 19198–19205.
25 E. Kalenius, M. Groessl and K. Rissanen, *Nat. Rev. Chem.*, 2019, **3**, 4–14.
26 T. Wyttenbach and M. T. Bowers, *J. Phys. Chem. B*, 2011, **115**, 12266–12275.
27 L. Shi, A. E. Holliday, H. Shi, F. Zhu, M. A. Ewing, D. H. Russell and D. E. Clemmer, *J. Am. Chem. Soc.*, 2014, **136**, 12702–12711.
28 L. Shi, A. E. Holliday, B. C. Bohrer, D. Kim, K. A. Servage, D. H. Russell and D. E. Clemmer, *J. Am. Soc. Mass Spectrom*, 2016, **27**, 1037–1047.
29 H. Tong, D. Bell, K. Tabei and M. M. Siegel, *J. Am. Soc. Mass Spectrom*, 1999, **10**, 1174–1187.
30 F. Lanucara, S. W. Holman, C. J. Gray and C. E. Eyers, *Nat. Chem.*, 2014, **6**, 281–294.
31 V. Gabelica and E. Marklund, *Curr. Opin. Chem. Biol.*, 2018, **42**, 51–59.
32 C. Bleiholder and F. C. Liu, *J. Phys. Chem. B*, 2019, **123**, 2756–2769.
33 J. Seo, W. Hoffmann, S. Warnke, X. Huang, S. Gewinner, W. Schollkopf, M. T. Bowers, G. von Helden and K. Pagel, *Nat. Chem.*, 2017, **9**, 39–44.
34 J. Seo, S. Warnke, K. Pagel, M. T. Bowers and G. von Helden, *Nat. Chem.*, 2017, **9**, 1263–1268.
35 V. Scutelnic, M. A. S. Perez, M. Marianski, S. Warnke, A. Gregor, U. Rothlisberger, M. T. Bowers, C. Baldauf, G. von Helden, T. R. Rizzo and J. Seo, *J. Am. Chem. Soc.*, 2018, **140**, 7554–7560.
36 F. S. Menges, E. H. Perez, S. C. Edington, C. H. Duong, N. Yang and M. A. Johnson, *J. Am. Soc. Mass Spectrom*, 2019, **30**, 1551–1557.
37 L. S. Shimizu, M. D. Smith, A. D. Hughes and K. D. Shimizu, *Chem. Commun.*, 2001, 1592–1593.
38 A. J. Sindt, M. D. Smith, P. J. Pellechia and L. S. Shimizu, *Cryst. Growth Des.*, 2018, **18**, 1605–1612.
39 J. Yang, M. B. Dewal, D. Sobransingh, M. D. Smith, Y. W. Xu and L. S. Shimizu, *J. Org. Chem.*, 2009, **74**, 102–110.
40 V. Gabelica, A. A. Shvartsburg, C. Afonso, P. Barran, J. L. P. Benesch, C. Bleiholder, M. T. Bowers, A. Bilbao, M. F. Bush, J. L. Campbell, I. D. G. Campuzano, T. Causon, B. H. Clowers, C. S. Creaser, E. De Pauw, J. Far, F. Fernandez-Lima, J. C. Fjeldsted, K. Giles, M. Groessl, C. J. Hogan, Jr., S. Hann, H. I. Kim, R. T. Kurulugama, J. C. May, J. A. McLean, K. Pagel, K. Richardson, M. E. Ridgeway, F. Rosu, F. Sobott, K. Thalassinos, S. J. Valentine and T. Wyttenbach, *Mass Spectrom. Rev.*, 2019, **38**, 291–320.
41 V. Gabelica, S. Livet and F. Rosu, *J. Am. Soc. Mass Spectrom*, 2018, **29**, 2189–2198.
42 A. Marchand, S. Livet, F. Rosu and V. Gabelica, *Anal. Chem.*, 2017, **89**, 12674–12681.
43 J. Ujma, K. Giles, M. Morris and P. E. Barran, *Anal. Chem.*, 2016, **88**, 9469–9478.
44 P. C. D. Hawkins, A. G. Skillman, G. L. Warren, B. A. Ellingson and M. T. Stahl, *J. Chem. Inf. Model.*, 2010, **50**, 572–584.
45 P. C. Hawkins and A. Nicholls, *J. Chem. Inf. Model.*, 2012, **52**, 2919–2936.
46 F. Weigend, *Phys. Chem. Chem. Phys.*, 2006, **8**, 1057–1065.
47 F. Weigend and R. Ahlrichs, *Phys. Chem. Chem. Phys.*, 2005, **7**, 3297–3305.
48 S. Grimme, J. Antony, S. Ehrlich and H. Krieg, *J. Chem. Phys.*, 2010, **132**, 154104.
49 J. Tomasi, B. Mennucci and R. Cammi, *Chem. Rev.*, 2005, **105**, 2999–3093.
50 M. J. Frisch, G. W. Trucks, H. B. Schlegel, G. E. Scuseria, M. A. Robb, J. R. Cheeseman, G. Scalmani, V. Barone, G. A. Petersson, H. Nakatsuji, X. Li, M. Caricato, A. V. Marenich, J. Bloino, B. G. Janesko, R. Gomperts, B. Mennucci, H. P. Hratchian, J. V. Ortiz, A. F. Izmaylov, J. L. Sonnenberg, D. Williams-Young, F. Ding, F. Lipparini, F. Egidi, J. Goings, B. Peng, A. Petrone, T. Henderson, D. Ranasinghe, V. G. Zakrzewski, J. Gao, N. Rega, G. Zheng, W. Liang, M. Hada, M. Ehara, K. Toyota, R. Fukuda, J. Hasegawa, M. Ishida, T. Nakajima, Y. Honda, O. Kitao, H. Nakai, T. Vreven, K. Throssell, J. J. A. Montgomery, J. E. Peralta, F. Ogliaro, M. J. Bearpark, J. J. Heyd, E. N. Brothers, K. N. Kudin, V. N. Staroverov, T. A. Keith, R. Kobayashi, J. Normand, K. Raghavachari, A. P. Rendell, J. C. Burant, S. S. Iyengar, J. Tomasi, M. Cossi, J. M. Millam, M. Klene, C. Adamo, R. Cammi, J. W. Ochterski, R. L. Martin, K. Morokuma, O. Farkas, J. B. Foresman and D. J. Fox, *Gaussian 09*, Gaussian, Inc., Wallingford, CT, 2016.
51 A. A. Shvartsburg and M. F. Jarrold, *Chem. Phys. Lett.*, 1996, **261**, 86–91.
52 M. F. Mesleh, J. M. Hunter, A. A. Shvartsburg, G. C. Schatz and M. F. Jarrold, *J. Phys. Chem.*, 1996, **100**, 16082–16086.
53 K. Sekimoto, N. Matsuda and M. Takayama, *Mass Spectrom.*, 2013, **2**, A0020.
54 T. D. Do, N. E. de Almeida, N. E. LaPointe, A. Chamas, S. C. Feinstein and M. T. Bowers, *Anal. Chem.*, 2016, **88**, 868–876.
55 S. L. Bernstein, N. F. Dupuis, N. D. Lazo, T. Wyttenbach, M. M. Condron, G. Bitan, D. B. Teplow, J. E. Shea, B. T. Ruotolo, C. V. Robinson and M. T. Bowers, *Nat. Chem.*, 2009, **1**, 326–331.
56 T. Dudev and C. Lim, *J. Am. Chem. Soc.*, 2000, **122**, 11146–11153.
57 N. J. Pace and E. Weerapana, *Biomolecules*, 2014, **4**, 419–434.
58 M. Laitaoja, J. Valjakka and J. Janis, *Inorg. Chem.*, 2013, **52**, 10983–10991.
59 C. Bleiholder, N. F. Dupuis, T. Wyttenbach and M. T. Bowers, *Nat. Chem.*, 2011, **3**, 172–177.
60 M. Schmidtmann, P. Coster, P. F. Henry, V. P. Ting, M. T. Wellere and C. C. Wilson, *CrystEngComm*, 2014, **16**, 1232–1236.
61 W. C. Schiessl, N. K. Summa, C. F. Weber, S. Gubo, C. Ducker-Benfer, R. Puchta, N. J. R. V. Hommes and R. van Eldik, *Z. Anorg. Allg. Chem.*, 2005, **631**, 2812–2819.

62 S. Warnke, J. Seo, J. Boschmans, F. Sobott, J. H. Scrivens, C. Bleiholder, M. T. Bowers, S. Gewinner, W. Schollkopf, K. Pagel and G. von Helden, *J. Am. Chem. Soc.*, 2015, **137**, 4236–4242.
63 D. C. Spellmeyer, A. K. Wong, M. J. Bower and J. M. Blaney, *J. Mol. Graphics Modell.*, 1997, **15**, 18–36.
64 M. T. McBride, T.-J. M. Luo and G. T. R. Palmore, *Cryst. Growth Des.*, 2000, **1**, 39–46.
65 I. J. Chen and N. Foloppe, *Bioorg. Med. Chem.*, 2013, **21**, 7898–7920.
66 A. S. Kamenik, U. Lessel, J. E. Fuchs, T. Fox and K. R. Liedl, *J. Chem. Inf. Model.*, 2018, **58**, 982–992.
67 P. Bonnet, D. K. Agrafiotis, F. Zhu and E. Martin, *J. Chem. Inf. Model.*, 2009, **49**, 2242–2259.
68 E. Perola and P. S. Charifson, *J. Med. Chem.*, 2004, **47**, 2499–2510.

